Wave-vector-dependent symmetry analysis of a photoemission matrix element: The quasi-one-dimensional model system Cu(110)(2×1)O

F. Pforte,[1] A. Gerlach,[1] A. Goldmann,[1] R. Matzdorf,[2] J. Braun,[3] and A. Postnikov[4]
[1]*Fachbereich Physik, Universität Kassel, Heinrich-Plett-Strasse 40, D-34132 Kassel, Germany*
[2]*Physikalisches Institut, Universität Würzburg, Am Hubland, D-97074 Würzburg, Germany*
[3]*Fachbereich Physik, Universität Münster, Wilhelm-Klemm-Strasse 9, D-48149 Münster, Germany*
[4]*Theoretische Tieftemperaturphysik, Universität Duisburg, D-47048 Duisburg, Germany*
(Received 31 July 2000; revised manuscript received 10 November 2000; published 27 March 2001)

We derive orbital symmetry character from the study of peak intensities in angle-resolved photoemission spectra taken at different incidence angles of *p*-polarized light. Our method of analysis is tested at the oxygen-derived antibonding band on the Cu(110)(2×1)O surface. This band has an initial state energy $E_i = -1.37$ eV ($T = 300$ K) at the $\bar{Y}$ point and shows even symmetry with respect to the ΓLUX mirror plane (along $\bar{\Gamma}\bar{Y}$). The intensity analysis reveals that orbitals both of *z*-like (along surface normal) and *y*-like symmetry (*y* along the Cu-O chains) are mixed into this band. This interpretation is supported by several calculations. The ground-state symmetry character was studied by a full-potential linearized augmented plane-wave method using a seven-layer supercell geometry. For a direct comparison with the experimental intensities, photoemission spectra at the $\bar{Y}$ point were calculated using the one-step model of photoemission. Our results contribute to a long-standing discussion about the orbital character of the even antibonding band. In particular we demonstrate that this kind of intensity analysis can supply valuable information about symmetry properties.

DOI: 10.1103/PhysRevB.63.165405 PACS number(s): 79.60.−i, 73.20.−r, 68.43.−h

I. INTRODUCTION

Today the interpretation of angle-resolved photoemission spectra (ARPES) from valence electron states of solids is being pushed past traditional limits. The determination of energy versus wave-vector dispersions $E(\mathbf{k})$ has become a standard method by now, and the resulting gain in knowledge about electronic properties is probably comparable to the role that neutron scattering played for the study of the elastic properties of solids. However, recent theoretical concepts go beyond the former independent-particle approximation used to derive just $E(\mathbf{k})$ from experimental peak positions. Many-body and strong correlation effects lead to distinct deviations from the one-electron picture, and these are reflected experimentally in peak shapes and line intensities see, e.g., Refs. 1–3. Recent interest focuses in particular on high-temperature superconductors and materials with reduced dimensionality such as quasi-one-dimensional metals.[4,5] These more exotic materials generally show a complex chemical composition, and it is often not trivial to prepare well-ordered surfaces and ensure the correct stoichiometry. Therefore new methods used to extract line-shape and line-intensity information from ARPES should be approved first by experience from well-understood materials.

In this context we have tried to extract relevant information from the experimental study of photoemission matrix elements. These are more sensitive to the involved wave functions and their symmetry character than the energy eigenvalues and they can be used to examine the wave functions from *ab initio* band-structure calculations. In order to check for its capabilities as well as for possible drawbacks, we study the even antibonding band at the Cu(110)(2×1)O surface along the $\bar{\Gamma}\bar{Y}$ azimuth of the surface Brillouin zone. The adsorbate system chosen is a well-known model system of surface science. It may provide understanding of the quasi-one-dimensional bonding along Cu-O chains, which can be also relevant to high-temperature copper oxide superconductors.

The atomic chemisorption of oxygen onto the Cu(110) surface has been extensively studied and good reviews with many references to earlier work can be found in Refs. 6 and 7. There is complete agreement that by exposure of molecular oxygen to Cu(110) at room temperature an ''added row'' structure is observed.[8] At a 0.5 monolayer coverage with atomic oxygen Cu-O rows are formed perpendicular to the close packed $[\bar{1}10]$ direction, with a distance $a\sqrt{2}$ between the rows, where *a* is the lattice constant of bulk Cu. In this (2×1)O structure the O($2p$) orbitals hybridize strongly with the Cu($3d$) states, forming bonding and antibonding linear combinations. The bonding orbitals are located at initial-state energies E_i between −8 and −4 eV (all energies are defined with respect to the Fermi energy E_F), whereas the antibonding contributions are located above $E_i = -4$ eV.[7,9] According to the C_{2v} point-group symmetry of the Cu(110)(2×1)O surface we expect *three* oxygen-derived wave-function symmetries *x* (oriented along the $[1\bar{1}0]$ bulk direction, i.e., along the $\bar{\Gamma}\bar{X}$ direction of the surface Brillouin zone), *y*($[001], \bar{\Gamma}\bar{Y}$) and *z* (along the surface normal). Due to the adsorption geometry[6–9] the dispersion of the oxygen-induced surface bands is strong along the rows. In contrast, only weak or even no dispersion is observed perpendicular to the rows, indicating only small inter-row interactions.

Three occupied bonding bands have been unanimously resolved in several experimental studies[7,10–12] and they appear (counting from the largest binding energy $|E_i|$ towards E_F) with symmetries *y*, *z*, and *x* at the $\bar{Y}$ point, located below

the *d* bands of the substrate. With respect to the band dispersion, there is also reasonable agreement between theory and experiment. For more details we refer to Refs. 7 and 9. There is, however, an ongoing controversy concerning the occupied antibonding adsorbate bands. Only *two* of them have been identified unambiguously[7,11–13] along the $\overline{\Gamma Y}$ direction. Their energies [symmetries with respect to the (*y, z*) mirror plane] at the $\overline{Y}$ point are $E_i=-1.37$ eV (even) and $E_i=-1.16$ eV (odd) with the sample at room temperature. There is also contradicting orbital assignment. While the band at $E_i=-1.16$ eV clearly shows *x*-like character, the even antibonding state at the $\overline{Y}$ point has been labeled *z*-like,[11] *y*-like,[12] or *y,z*.[7] All assignments are also supported by (different) calculations. Two theoretical investigations based on tight-binding linear combination of atomic orbitals (LCAO) methods[14] and self-consistent slab calculations[15,16] reveal a third antibonding band associated with *y* symmetry. This third band, however, was never detected experimentally. A more recent calculation based on density-functional theory[9] reveals two antibonding oxygen bands below E_F at the $\overline{Y}$ point with orbital symmetries *z* and *x*, respectively. This calculation predicts, however, that several other O(p_z) bands should be formed. The reason for this complexity is that the orbitals hybridize with both the Cu atoms within the added row and with subsurface Cu atoms due to the large vertical extension of the p_z orbitals. In conclusion, the present understanding of the antibonding bands is quite unsatisfactory.

In order to gain additional information we study in the present paper the emission intensity of the antibonding band at $E_i=-1.37$ eV as observed in angle-resolved photoelectron spectra. From a detailed analysis we derive the relative size of the *y* and *z* components of the photoemission matrix element. These results are compared with corresponding data obtained from an intensity calculation based on the one-step model of photoemission. Basically good agreement is obtained. Additionally our results demonstrate that the use of Fresnel's equations combined with empirically derived effective dielectric constants enable a heuristic but successful description of the surface optical properties.

II. EXPERIMENTAL DETAILS

Our UHV chamber working with a base pressure below 10^{-10} mbar is equipped with all standard facilities for sample preparation. The Cu(110) substrate was prepared by cycles of argon-ion bombardment ($E_{\rm kin}=500$ eV) and annealing. With the sample at $T=300$ K we admitted 20 L (1 L=1 Langmuir=10^{-6} Torr s) of O_2, which results in a saturated atomic adlayer of half-monolayer coverage. This structure still contains steps, domain boundaries, and other types of defects.[6] It was therefore annealed to $T=640$ K for some minutes. This treatment leads to large flat terraces.[6] The success of the annealing procedure could be monitored *in situ* by observation of a considerable narrowing of the photoemission lines from the two antibonding adsorbate bands.

In our arrangement (see Fig. 1 for the definition of the coordinates and angles) photoelectron spectra are measured along the *y* azimuth ($\overline{\Gamma Y}$) by rotating the crystal through the *x* axis, while the electron energy analyzer is fixed.[17] Two different photon sources with $\hbar\omega=21.2$ eV have been used in this experiment. In the first setup the angle $\psi+\theta=45°$ between light incidence and detected electrons is constant. The surface normal, electron emission direction, and direction of incident photons are confined to the same (*y,z*) optical plane. The incident light is polarized linearly by triple reflection[18] from gold mirrors, which we produced by sputtering of gold onto polished glass surfaces at elevated temperature. This three-mirror system may be rotated around the axis of light incidence by 360°, thereby allowing us to switch between *s* polarization (electric field vector parallel to *x*) and *p* polarization. The second photon source produces exclusively *p*-polarized light; for details see Ref. 17. It may be rotated by 360° around the manipulator axis. This arrangement allows us to vary the light incidence angle ψ of the *p*-polarized light with the exception of ±15° around the electron take-off direction, when the polarizer blocks the lens entrance at fixed electron escape angle θ. The energy resolution of the electron energy analyzer is tunable down to $\Delta E=10$ meV. The entrance lens contains a pinhole of variable diameter that allows the *in situ* variation of the angular resolution between $\Delta\theta=\pm0.4°$ and ±2°. For details we refer the reader to Ref. 17.

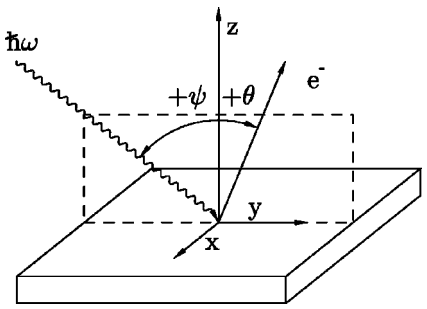

FIG. 1. Experimental geometry indicating the definition of angles and Cartesian coordinates. For angle-dependent measurements the crystal is rotated through the manipulator axis (*x* direction). The angles ψ and θ are defined with respect to the sample normal. In all experiments reported below *y* is parallel to the bulk [001] direction ($x\|[1\bar{1}0]$).

III. EXPERIMENTAL RESULTS

A. Overview

Figure 2 shows typical results taken with the antibonding bands a_x and a_{yz} at the $\overline{Y}$ point of the surface Brillouin zone. The dotted curves represent spectra excited from the clean substrate with $\hbar\omega=21.2$ eV. The solid lines refer to Cu(110)(2×1)O at the saturation coverage with 0.5 monolayers of atomic oxygen. It causes the bonding bands labeled *b* and the antibonding bands labeled *a*. Our spectra are much better resolved and reveal more fine-structure details, but they are basically in very good agreement with those presented in Ref. 7. Still we are not able to resolve the missing

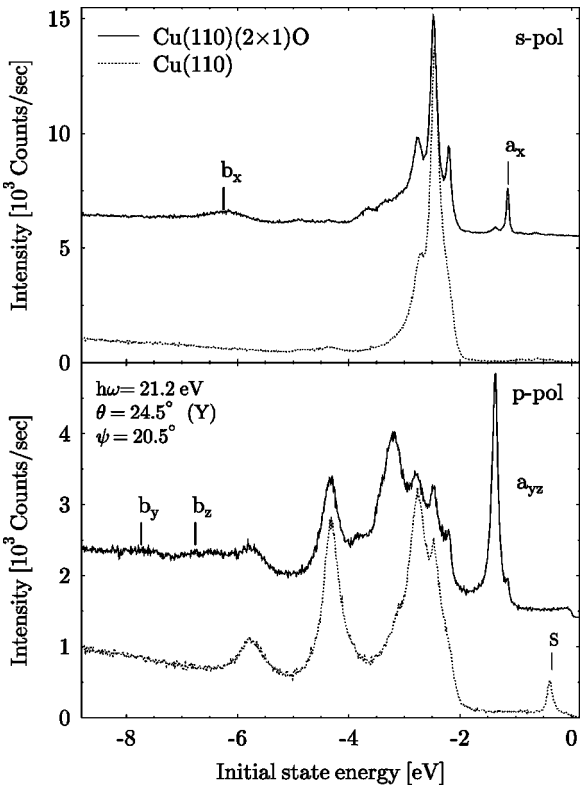

FIG. 2. Photoelectron spectra from clean Cu(110), dotted lines, and Cu(110)(2×1)O, solid lines, taken with linearly polarized light at $\hbar\omega = 21.2$ eV. At $\theta = 24.5°$ the antibonding bands a_x, a_{yz} are located just at the $\bar{Y}$ point of the surface Brillouin zone. The label *S* refers to the Shockley surface state. Bonding bands identified earlier (Refs. 7 and 10–12) are labeled b_y, b_z, and b_x, respectively. All intensities are reproduced as measured at constant photon flux. Resolution parameters $\Delta\theta = \pm 1°$, $\Delta E = 21$ meV with the sample at $T = 140$ K.

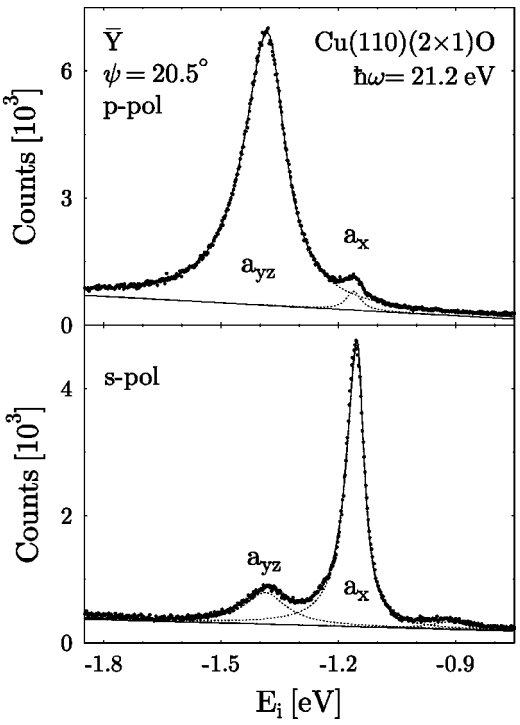

FIG. 3. Antibonding bands at Cu(110)(2×1)O labeled a_{yz} and a_x in Fig. 2 observed in high-resolution scans with *p*-polarized (top) and *s*-polarized (bottom) light (polarization 86%). The sample temperature was 130 K; resolution parameters are $\Delta\theta = \pm 1°$, $\Delta E = 18$ meV.

third antibonding band between E_F and the top of the Cu *d* bands. Our assignments of the bands *b* are in complete agreement with Ref. 7.

Figure 3 shows the polarization dependence of the oxygen-derived antibonding doublet around $E_i = -1.3$ eV obtained from a high-resolution scan. This pair of odd and even emission lines clearly exhibits slightly asymmetric Lorentzian line shapes (as shown by the fitting curves through the data points) of dramatically different widths. The asymmetry can be quantitatively traced back to our still finite angular resolution $\Delta\theta$. This was verified by data taken at different $\Delta\theta$ and by calculations taking the measured dispersion into account: Around the $\bar{Y}$ point both bands disperse to the left in Fig. 3 and finite $\Delta\theta$ results in some broadening on the left wing. The different widths of a_x and a_{yz} peaks result from different photohole lifetimes.[13]

The two states shown in Fig. 3 represent an excellent test object for the proper performance of the polarizers. Their energy distance is about 0.21 eV, which is large compared with the spin-orbit coupling parameter $\zeta = 0.08$ eV of Cu. Therefore we expect negligible mixing of symmetries *x* and *y,z*. In consequence the remaining intensity ratios of a_x and a_{yz} are essentially due to the finite degree of polarization. The analysis of Fig. 3 gives a linear polarization of 86 ±3 % for the first polarizer, which has to be compared with 91% calculated on the basis of the optical constants of Au. We consider this agreement satisfying because the calculation does not account for residual contamination of the gold mirrors and, in particular, assumes that the mirrors are perfectly flat on the lateral scale of the light wavelength ($\lambda = 58$ nm). Turning the arguments around we may deduce that any symmetry mixing by spin-orbit coupling results in an intensity contribution of less than 5%.

B. Intensity analysis

In the standard description of photoemission the transition matrix element from the initial state at E_i to the final state at $E_f = E_i + \hbar\omega$ can be written in the dipole approximation as[19]

$$M_{fi} \propto \langle f|\mathbf{A}\cdot\mathbf{p}|i\rangle \approx \mathbf{A}\cdot\langle f|\mathbf{p}|i\rangle = \mathbf{A}\cdot\mathbf{P}_{fi}, \qquad (1)$$

where **A** is the vector potential of the light and **p** is the momentum operator. The momentum matrix element $\mathbf{P}_{fi}$ is a complex vector that depends only on the initial and final states. By variation of **A**, which may be calculated from the incident light by Fresnel's equations,[20–22] we can determine the relative size of its real and imaginary parts experimentally. In what follows we use only *p*-polarized light ($A_x = 0$). Thus the photoemission intensity *I* can be written as a function of light incidence angle ψ (compare Fig. 1) as

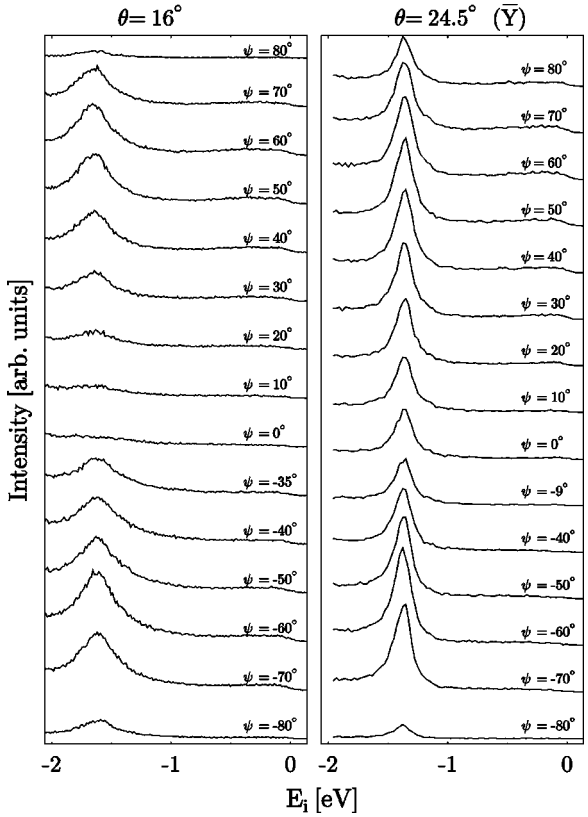

FIG. 4. Photoemission spectra of the antibonding band a_{yz} taken at fixed electron emission angle θ along the $\bar{\Gamma}\bar{Y}$ direction of the surface Brillouin zone. The parameter ψ is the angle of incidence with respect to the surface normal of 94% *p*-polarized incident photons at $\hbar\omega = 21.2$ eV. Left: $\theta = 16°$, resolution parameters $\Delta\theta = 1.5°$, $\Delta E = 21$ meV; right: $\theta = 24.5°$, $\Delta\theta = 1°$, $\Delta E = 28$ meV. All intensities refer to the same incident photon flux.

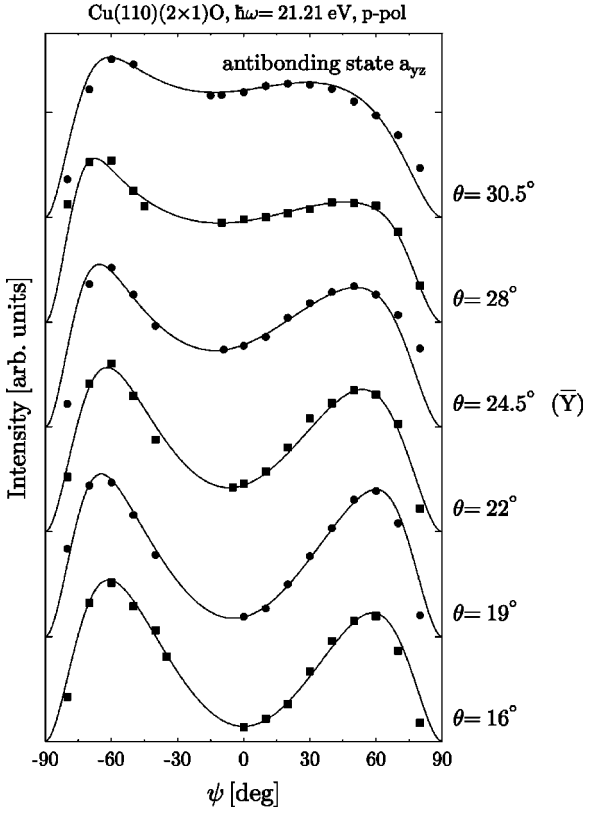

FIG. 5. Peak a_{yz} intensities taken at different electron escape angle θ as a function of light-incidence angle ψ. Symbols are experimental data extracted from spectra like those shown in Fig. 4. Solid lines represent fits to the data used for the determination of $\mathbf{P}_{fi}$ according to Eq. (2).

$$I(\psi) \propto |M_{fi}|^2 = |A_y(\psi) P_y^* + A_z(\psi) P_z^*|^2, \tag{2}$$

where P^* are the complex conjugate components of $\mathbf{P}_{fi}$. Within our treatment we express the components of the momentum matrix element as $P_z = |\mathbf{P}_{fi}| \cos\beta$ and $P_y = |\mathbf{P}_{fi}| \sin\beta e^{i\gamma}$, where β is the angle between $\mathbf{P}_{fi}$ and the surface normal and γ accounts for a phase shift between P_y and P_z. For more details we refer the reader to Ref. 22.

Figure 4 shows photoemission spectra of the antibonding state a_{yz} for different light-incident angles ψ at two different electron emission angles θ (left and right panel, respectively). The variation of peak intensity as a function of ψ is easily visible. In order to analyze $I(\psi)$ we take only the peak maximum amplitudes, because the peak width at fixed θ does not change with ψ. In addition, no separation from a_x is required (compare Fig. 3). Results from the antibonding a_{yz} state taken at different θ are shown in Fig. 5 as filled squares or circles. These intensities have been normalized to equal maximum amplitude, because our analysis checks only for the shape of $I(\psi)$. In fact it is extremely difficult to measure all experimental parameters relevant for the determination of the absolute value of $\mathbf{P}_{fi}$. In contrast, β can be determined reliably and will be relevant for a comparison with the theoretical results. The physical content of β is transparent: $\beta = 0$ means that $\mathbf{P}_{fi}$ is oriented along the surface normal. In this case $I(0) = 0$ and $I(+\psi) = I(-\psi)$. In contrast, if $\beta = 90°$ $I(\psi)$ must be symmetric with a maximum at $\psi = 0$. Of course $I \to 0$ for $\psi \to \pm 90°$, because the light is totally reflected and no photoemission occurs. Let us now inspect Fig. 4. The left panel indicates that $I(\psi)$ gets small at $\psi = 0$, but no full $\pm\psi$ symmetry is observed. This shows that $\mathbf{P}_{fi}$ is oriented near normal, but a finite component P_y remains. At $\theta = 24.5°$ ($\bar{Y}$ point) we observe much more intensity at $\psi = 0$. This indicates an increased ratio P_y/P_z compared to $\theta = 16°$. We have fitted Eq. (2) to the data collected in Fig. 5. The quality of these fits can be checked by comparing the calculated $I(\psi)$ curves (solid lines) with the measured intensities (symbols). The fit parameter β is plotted in its dependence on the electron wave vector parallel to the surface as shown in Fig. 6. As is evident, it depends strongly on $k_\parallel$.[24] The a_{yz} band contains both orbital symmetries *y* and *z*, with an increasing weight of *y* for larger $k_\parallel$ (compare Secs. IV A and IV B for further discussion). The data shown in Fig. 6 do not contradict the possibility that the matrix element is exclusively given by P_z at $k_\parallel = 0$, but the vanishing slope of $\beta(k_\parallel)$ on approaching the zone center suggests a non-negligible contribution of P_y at the $\bar{\Gamma}$ point. Indeed inspection of polarization-dependent photoemission spectra (Figs. 3 and 7 in Ref. 7) gives strong evidence that also at normal emission the even antibonding band is heavily mixed of *y*- and *z*-like orbitals.[25]

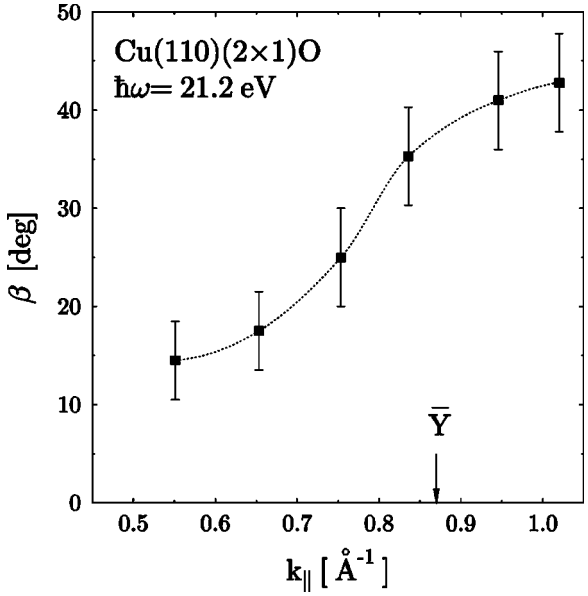

FIG. 6. Direction β of the momentum matrix element $\mathbf{P}_{fi}$ with respect to the surface normal in dependence on $k_{\parallel}$ along $\bar{\Gamma}\bar{Y}$. Data points from fits shown in Fig. 5; the dotted line is drawn as a guide for the eye.

As mentioned already the solid lines in Fig. 5 result from a fit of Eq. (2) to the data points. We used Fresnel's equations to compute $A_y(\psi)$ and $A_z(\psi)$. It turned out, however, that the use of the bulk optical constant $\varepsilon=0.63+i0.74$ of Cu (Ref. 23) did not result in a satisfactory fit. Therefore we treated ε as an additional fit parameter. The solid lines shown in Fig. 5 are the best fit, obtained with $\varepsilon=0.94+i0.24$. The typical error is ± 0.1 for both ε_1 and ε_2. This value of ε is intermediate between the vacuum value $\varepsilon=1$ and the bulk data, and we consider this parameter (in combination with the Fresnel equations) as an empirical and pragmatic approach to account for local-field effects related with the selvedge.[19] We note that the use of the two different ε's does not change β beyond the error bars.

IV. CALCULATIONS

A. Qualitative considerations

The considerable increase of β with $k_{\parallel}$ as observed in Fig. 6 does not simply reflect a variation of the relative orbital contributions in the wave function. Generally the wave function along the one-dimensional (1D) chain may be written as a Bloch function $\varphi(\mathbf{r})=u_{k_y}(\mathbf{r})\exp(ik_y y)$, where k_y is the wave vector parallel to the Cu-O chain. All properties along x and z are included in $u(\mathbf{r})$. If we assume such a description for both initial (i) and final (f) states of a photoemission process, the momentum matrix element is given by

$$\mathbf{P}_{fi}\propto\langle u_f(\mathbf{r})\exp(ik_y y)|\mathbf{p}|u_i(\mathbf{r})\exp(k_y y)\rangle. \tag{3}$$

The differentiation according to the momentum operator $\mathbf{p}=-i\hbar\nabla$ results in some asymmetry due to the phase factor $\exp(ik_y y)$. While we obtain $P_z\propto\langle u_f\exp(ik_y y)|(\partial u_i/\partial z)\exp(ik_y y)\rangle$ and similarly for P_x, a second term is obtained for P_y:

$$P_y\propto\langle u_f\exp(ik_y y)|(\partial u_i/\partial y)\exp(ik_y y)\rangle + ik_y\langle u_f\exp(ik_y y)|u_i\exp(ik_y y)\rangle. \tag{4}$$

Consequently there is, besides contributions to $\partial u_i/\partial y$ from orbital components of yz-like symmetry, an additional contribution from the second term of the last equation, which gains increasing weight with $k_{\parallel}$.

At $k_{\parallel}=0$, however, the phase factor drops out and a combination of atomic orbitals may be used to illustrate the composition of the wave function within a linear chain of Cu-O atoms. If we describe oxygen by the $2p_x$,$2p_y$,$2p_z$ orbitals and copper by its $3d$ orbitals of symmetry d_{xy}, d_{yz}, d_{xz}, d_{y^2}, and $d_{x^2-z^2}$, a textbook LCAO calculation yields the following results: In an isolated chain p-d hybridization results in a mixture of $|x,xy\rangle$, $|z,yz\rangle$, and $|y,y^2\rangle$. The first and second states are energetically degenerate. However, $|xz\rangle$ and $|x^2-z^2\rangle$ do not mix. If the chain is put on a substrate, the symmetry is broken and the potential $V(z)$ along the surface normal is no longer symmetric: $V(z)\neq V(-z)$. Now the degeneracy between $|x,xz\rangle$ and $|z,yz\rangle$ is lifted. This reflects the experimentally observed splitting between the antibonding bands labeled yz and x in Fig. 2. Moreover, $|z,yz\rangle$ and $|y,y^2\rangle$ hybridize, while $|x,xy\rangle$ and $|y,y^2\rangle$ do not mix. In conclusion, already this oversimplified linear chain model predicts contributions of both matrix element components P_y and P_z, in accord with the experimental result shown in Fig. 6.

B. Calculation of the electronic structure

The aim of our present calculations is twofold: to look in more detail at the dispersion of O($2p$)-related bands in the surface Brillouin zone, making use of an all-electron method of superior accuracy, and to calculate the photocurrent at the excitation energies and escape angles relevant for a direct comparison with the ARPES results. For the first of these tasks, we utilize the full-potential linearized augmented plane-wave method (FLAPW), well suited for the study of open structures and surfaces, as implemented in the WIEN97 package.[26] A supercell geometry is used, with a mirror-symmetric slab of seven [110] layers representing bulk Cu and Cu-O chains on top of it on both sides. The slabs are separated by empty spaces corresponding to six interlayer distances (measured between the Cu-O chains). The atomic sphere sizes are $R_{\mathrm{MT}}=1.8$ a.u. for Cu and 1.6 a.u. for O. Since the exact total energy evaluation for the structure optimization is not our goal, a moderate value of the parameter $R_{\mathrm{MT}}K_{\max}=8$ determining the plane-wave cutoff is applied. The exchange correlation is treated in the generalized gradient approximation after Perdew, Burke, and Ernzerhof.[27] The positions of atoms at the reconstructed and relaxed (within the two uppermost Cu layers and the Cu-O chains above) surface are taken from an impact-collision ion-scattering spectroscopy study.[28] Other estimations of the details of relaxation are published (see, e.g., Table 6 of Ref. 9 for an

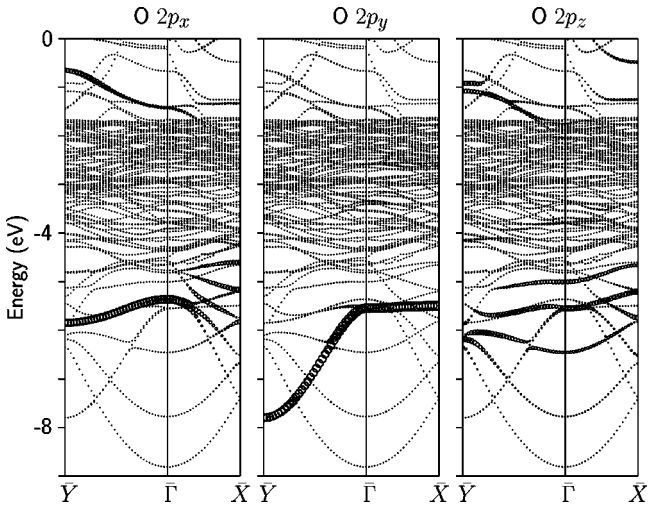

FIG. 7. Oxygen-derived band dispersions along $\overline{\Gamma Y}$ and $\overline{\Gamma X}$ from present FLAPW calculations. The size of the circles represents the relative strength of the orbital contribution indicated on top of each panel.

overview), but we do not expect the overall trends in the band dispersion to be very sensitive to small changes.

Our FLAPW results for the energy band dispersion along both $\overline{\Gamma Y}$ and $\overline{\Gamma X}$ directions are shown in Fig. 7. The contributions of the O($2p_x$,$2p_y$,$2p_z$) states in corresponding eigenvectors are represented by the size of circles (in arbitrary units but in the same scale in all three panels). The dispersion of the O($2p$) states is essentially confined to the direction along the chains, as could be expected, and how it has been discussed previously on the basis of available experimental data (see, e.g., Refs. 7 and 29). The strong O($2p_y$)-Cu($3d$) hybridization shifts the bonding component of corresponding states well below the bulk of the Cu *d* band at the $\bar{Y}$ point, where it remains well localized at the oxygen atom and could be detected experimentally. The corresponding antibonding band floats above the Fermi level, is much more diffuse and has a (not so well pronounced) maximal participation of the O($2p$) states at about 6 eV. Essentially this has been already shown in the scheme of O($2p$) dispersion in Ref. 9. Our calculation demonstrates that the O($2p_y$)-bonding band disperses strongly along $\overline{\Gamma Y}$, merges the bottom of the Cu *d* band at $\bar{\Gamma}$ and shows no dispersion along $\overline{\Gamma X}$. It behaves in a rather complex way (actually dependent on the inclusion of additional Cu layers in the supercell), so that its position near the zone center cannot be quite clearly traced.

The dispersion of the O($2p_x$)- and O($2p_z$)-related bands along the $\overline{\Gamma Y}$ line is much smaller and produces both bonding and antibonding contributions below the Fermi level. The antibonding states at the $\bar{Y}$ point are clearly split off from the Cu *d* band and are quite well localized on oxygen. In agreement with experimental observation (Fig. 3), the top of the O($2p_x$)-antibonding band at the $\bar{Y}$ point lies by approximately 0.3 eV higher than the O($2p_z$) band.

In order to gain further insight, we have also calculated the $k_{\|}$-resolved density-of-states contributions from other orbital symmetries localized on the Cu-O chains. No significant contributions from Cu($4s$) and Cu($4p$) were found. However, *d* admixtures to both antibonding bands along $\overline{\Gamma Y}$ are of considerable strength. The even antibonding band a_{yz} has a dominant component of symmetry $|yz\rangle$ all along $\overline{\Gamma Y}$. In contrast, the contribution of $|z^2\rangle$ is weak around the $\bar{\Gamma}$ point and almost negligible on approaching $\bar{Y}$. There is also a significant contribution of symmetry $|xy\rangle$ to the antibonding band labeled a_x in the experimental data. Neither $|xz\rangle$ nor $|x^2-y^2\rangle$ copper orbitals are significantly admixed into a_x and a_{yz}. Interestingly the intense oxygen-induced feature observed with *p*-polarized light at $E_i=-3.22$ eV within the *d* bands of Cu (lower panel of Fig. 2) is of predominant $|x^2-y^2\rangle$ symmetry. This assignment can be verified experimentally: Spectra taken at small light-incidence angle exhibit enhanced intensity of this peak, but the structure is almost invisible with *s*-polarized light, in accordance with the calculated symmetry character.

C. Calculation of the photocurrent

The calculation is based on the scattering formalism and the one-step model of photoemission. In order to reduce the computational effort we did not use the accurate potentials (as obtained in a FLAPW calculation) near the atoms and at the interstitial positions. It proved to be much more practical (and tolerable with regard to the accuracy of final results) to accept the geometry of space-filling (overlapping) spheres, with spherically averaged potentials inside. Along with spheres centered at copper and oxygen atoms, a number of empty spheres was introduced to pack the space between the Cu-O chains and in the vacuum region. Otherwise the slab geometry as described above for the FLAPW calculation was used. The self-consistent calculation of corresponding potentials has been done by the linear muffin-tin orbitals method[30] in its tight-binding (TB) implementation.[31] An attempt has been made to imitate as greatly as possible (by the choice of sizes and positions of empty spheres) the dispersion obtained in a more accurate FLAPW calculation. The local density of states calculated by the TB LMTO method turned out to be quite robust against these small changes and in all cases agreed well with that shown in Fig. 5 of Ref. 9. The spectroscopic analysis is based on a relativistic one-step model of photoemission,[32] which is a generalization of Pendry's formula for the photocurrent.[33,34] It allows for calculating spin-integrated and spin-resolved photoemission spectra from pure elemental solids and compounds.

Some remarks concerning the spectroscopic analysis are necessary. At first we have included lifetime effects in the final and initial states in a phenomenological way using a parametrized complex inner potential $V_0(E)=V_{0r}(E)+iV_{0i}(E)$. The real part serves as a reference energy inside the crystal with respect to the vacuum level. For the final state a constant imaginary part $V_{0i}(E_2)=1.8$ eV has been chosen. For the initial state a weakly energy-dependent pure imaginary part $V_{0i}(E_1)=\arctan(0.01+0.01E^2)$ was used. This energy dependence reflects semiquantitatively the decreasing lifetime of hole states with increasing binding energy. A realistic description of the surface potential was

guaranteed through a Rundgren-Malström barrier,[37] optimized for Cu. Furthermore, the slab geometry used to determine the Cu(110)(2×1)O adsorbate system requires a special layer structure in order to describe the semi-infinite crystal, from which the photocurrent results. This is due to the layer Korringa-Kohn-Rostoker (KKR) multiple scattering formalism,[35,36] usually applied in a photoemission analysis. Including the surface layer, four different types of layers must be classified as overlayers on the Cu(110) bulk crystal. Moreover, reconstruction and relaxation effects in the surface were considered by the rumpled-layer concept[35] known from multiple scattering theory. Because of this complicated layer structure we restricted ourselves to a muffin-tin-based photoemission analysis, which turned out to be sufficient for a first comparison with the experimental data taken at the $\overline{Y}$ point of the surface Brillouin zone. A detailed analysis concerning the dispersion behavior of the different oxygen states would require a full-potential scheme.

Our one-step-model calculations do not allow direct access to single-particle matrix elements. Therefore the photocurrent $I(E_i)$ at $\hbar\omega = 21.2\,\mathrm{eV}$ and several electron exit angles θ has been calculated with the p polarization of the incoming radiation taken properly into account. To be consistent we used Fresnel's equations with the empirically adjusted experimental ε_1 and ε_2 as mentioned above. The calculated spectra were then analyzed by the same procedure as the experimental ones, resulting in ''theoretical'' $I(\psi)$ curves. The result at the $\overline{Y}$ point is reproduced in Fig. 8. While there is qualitative overall agreement there still exist quantitative discrepancies. The experimental data result in $\beta = 35° \pm 5°$ and $\gamma = -72° \pm 10°$. From the fit to the calculated $I(\psi)$ points we obtain $\beta = 22° \pm 5°$ and $\gamma = -74° \pm 10°$. We consider this as a reasonable agreement, i.e., the one-step-model calculation reproduces the experimental matrix element reasonably well.

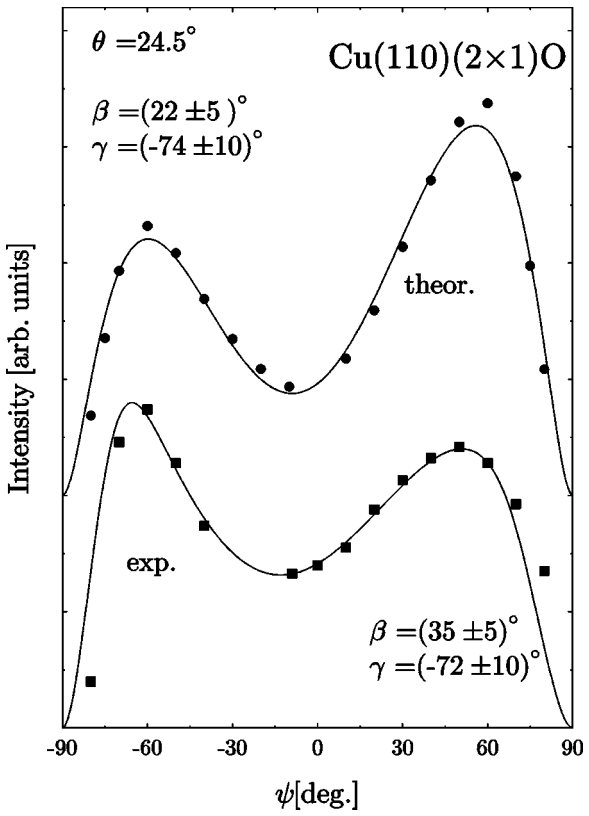

FIG. 8. Intensity of the antibonding band a_{yz} in its dependence on the light-incidence angle ψ as observed experimentally (bottom) and calculated (top). For details see text.

V. SUMMARY AND CONCLUSIONS

We have determined the orbital symmetry of the antibonding bands along $\overline{\Gamma Y}$ by a detailed intensity analysis and calculations. The odd band a_x, which is observed experimentally only with *s*-polarized light, is essentially composed of $O(2p_x)$ and $Cu(3d_{xy})$ wave functions. The antibonding band a_{yz}, which is observed with *p*-polarized light, contains significant $O(2p_z)$ character, but essentially no $O(2p_y)$ contribution. *y*-like symmetry is introduced by intense mixing with $Cu(3d_{yz})$ orbitals. Probably this contribution results in a nonvanishing component P_y at $k_\parallel = 0$ and enters the momentum matrix element also off-normal. These results resolve the controversy regarding the symmetry of the even antibonding band. Over the full $k_\parallel$ range from $\overline{Y}$ to halfway between $\overline{\Gamma}$ and $\overline{Y}$, this band is of mixed *y,z* symmetry.

Speaking more generally we have demonstrated at the model system Cu(110)(2×1)O that relevant symmetry information can be obtained from an inspection of intensities measured as a function of the light-incidence angle. Our analysis shows that both the matrix element components P_y and P_z contribute to the intensity of transitions from the even band along $\overline{\Gamma Y}$. A more quantitative result, however, requires support from high-quality electronic structure calculations. Nevertheless, the study of momentum matrix elements may add relevant information to our understanding of surface electronic properties.

ACKNOWLEDGMENT

Our work is continuously supported by the Deutsche Forschungsgemeinschaft (DFG).

[1] M. Hengsberger, D. Purdie, P. Segovia, M. Garnier, and Y. Baer, Phys. Rev. Lett. **83**, 592 (1999).

[2] T. Valla, A. V. Fedorov, P. D. Johnson, B. O. Wells, S. L. Hulbert, Q. Li, G. D. Gu, and N. Koshizuka, Science **285**, 2110 (1999).

[3] S. LaShell, E. Jensen, and T. Balasubramanian, Phys. Rev. B **61**, 2371 (2000).

[4] P. V. Bogdanov, A. Lanzara, S. A. Kellar, X. J. Zhou, E. D. Lu, W. J. Zheng, G. Gu, J.-I. Shimoyama, K. Kishio, H. Ikeda, R. Yoshizaki, Z. Hussain, and Z. X. Shen, Phys. Rev. Lett. **85**, 2581 (2000).

[5] J. Voit, L. Perfetti, F. Zwick, H. Berger, G. Margaritondo, G. Grüner, H. Höchst, and M. Grioni, Science **290**, 501 (2000).

[6] F. Besenbacher and J. K. Norskov, Prog. Surf. Sci. **44**, 5 (1993).

[7] R. Courths, S. Hüfner, P. Kemkes, and G. Wiesen, Surf. Sci. **376**, 43 (1997).
[8] D. J. Coulman, J. Wintterlin, R. J. Behm, and G. Ertl, Phys. Rev. Lett. **64**, 1761 (1990).
[9] S. Y. Liem, G. Kresse, and J. H. R. Clarke, Surf. Sci. **415**, 194 (1998).
[10] R. A. DiDio, D. M. Zehner, and E. W. Plummer, J. Vac. Sci. Technol. A **2**, 852 (1984).
[11] R. Courths, B. Cord, H. Wern, H. Saalfeld, and S. Hüfner, Solid State Commun. **63**, 619 (1987).
[12] R. Ozawa, A. Yamane, K. Morikawa, M. Ohwada, K. Suzuki, and H. Fukutani, Surf. Sci. **346**, 237 (1996).
[13] R. Matzdorf and A. Goldmann, Surf. Sci. **412/413**, 61 (1998).
[14] L. H. Tjeng, M. B. J. Meinders, and G. A. Sawatzky, Surf. Sci. **233**, 163 (1990).
[15] B. Weimert, J. Noffke, and L. Fritsche, Surf. Sci. **264**, 365 (1992).
[16] B. Weimert, J. Noffke, and L. Fritsche, Vacuum **41**, 163 (1990).
[17] R. Matzdorf, A. Gerlach, R. Hennig, G. Lauff, and A. Goldmann, J. Electron Spectrosc. Relat. Phenom. **94**, 279 (1998).
[18] K. Jacobi, R. Geng, and W. Ranke, J. Phys. E **11**, 982 (1978).
[19] S. Hüfner, *Photoelectron Spectroscopy—Principles and Applications*, Springer Series in Solid-State Science (Springer, Berlin, 1995), Vol. 82.
[20] M. Born and E. Wolf, *Principles of Optics* (Pergamon, Oxford, 1970).
[21] M. A. B. Whitaker, J. Phys. C **11**, L151 (1978).
[22] A. Gerlach, R. Matzdorf, and A. Goldmann, Phys. Rev. B **58**, 10 969 (1998).
[23] H. J. Hagemann, W. Gudat, and C. Kunz, J. Opt. Soc. Am. **65**, 742 (1975).
[24] We are unable to determine β at $k_{\|}<0.5\,\text{Å}^{-1}$: The antibonding a_{yz} band disperses rapidly to larger $|E_i|$ and immerses into the *d*-band region around normal emission $(\overline{\Gamma})$, thus making an intensity determination unreliable.
[25] We have performed a similar analysis with $\hbar\omega=10.6$ eV (krypton resonance radiation) around the $\overline{Y}$ point. The results for β agree within the error bars with those reproduced in Fig. 6.
[26] P. Blaha, K. Schwarz, and J. Luitz, WIEN97 (Vienna University of Technology, Vienna, 1997), improved and updated UNIX version of the original copyrighted WIEN code, which was published by P. Blaha, K. Schwarz, P. Sorantin, and S. B. Trickey, Comput. Phys. Commun. **59**, 339 (1990).
[27] J. P. Perdew, K. Burke, and M. Ernzerhof, Phys. Rev. Lett. **77**, 3865 (1996).
[28] H. Dürr, Th. Fauster, and R. Schneider, Surf. Sci. **244**, 237 (1991).
[29] K. Stahrenberg, Th. Herrmann, N. Esser, and W. Richter, Phys. Rev. B **61**, 3043 (2000).
[30] O. K. Andersen, Phys. Rev. B **12**, 3060 (1975).
[31] O. K. Andersen and O. Jepsen, Phys. Rev. Lett. **53**, 2571 (1984).
[32] J. Braun, Rep. Prog. Phys. **59**, 1267 (1996).
[33] J. B. Pendry, Surf. Sci. **57**, 679 (1976).
[34] J. F. L. Hopkinson, J. B. Pendry, and D. J. Titterington, Comput. Phys. Commun. **5**, 599 (1980).
[35] J. B. Pendry, *Low Energy Electron Diffraction* (Academic, London, 1974).
[36] R. Feder, J. Phys. C **14**, 2049 (1981).
[37] G. Malmström and J. Rundgren, Comput. Phys. Commun. **19**, 263 (1980).